2D Materials

PAPER

Raman imaging of twist angle variations in twisted bilayer graphene at intermediate angles

To cite this article: A Schäpers *et al* 2022 *2D Mater.* **9** 045009

IOP Publishing 2D Mater. **9** (2022) 045009 https://doi.org/10.1088/2053-1583/ac7e59

2D Materials

RECEIVED
8 March 2022

REVISED
13 June 2022

ACCEPTED FOR PUBLICATION
5 July 2022

PUBLISHED
18 July 2022

PAPER

Raman imaging of twist angle variations in twisted bilayer graphene at intermediate angles

A Schäpers[1,7], **J Sonntag**[1,2,7], **L Valerius**[1], **B Pestka**[3], **J Strasdas**[3], **K Watanabe**[4], **T Taniguchi**[5], **L Wirtz**[6], **M Morgenstern**[3], **B Beschoten**[1,*], **R J Dolleman**[1] and **C Stampfer**[1,2]

[1] JARA-FIT and 2nd Institute of Physics, RWTH Aachen University, 52074 Aachen, Germany
[2] Peter Grünberg Institute (PGI-9), Forschungszentrum Jülich, 52425 Jülich, Germany
[3] 2nd Institute of Physics B and JARA-FIT, RWTH Aachen University, 52074 Aachen, Germany
[4] Research Center for Functional Materials, National Institute for Materials Science, 1-1 Namiki, Tsukuba 305-0044, Japan
[5] International Center for Materials Nanoarchitectonics, National Institute for Materials Science, 1-1 Namiki, Tsukuba 305-0044, Japan
[6] Department of Physics and Materials Science, University of Luxembourg, 162a avenue de la Faïencerie, L-1511 Luxembourg, Luxembourg
[7] These authors contributed equally.
[*] Author to whom any correspondence should be addressed.

E-mail: bernd.beschoten@physik.rwth-aachen.de

Keywords: Raman spectroscopy, acoustic phonons, zone folding, graphene, twisted bilayer graphene

Supplementary material for this article is available online

Abstract

Van der Waals layered materials with well-defined twist angles between the crystal lattices of individual layers have attracted increasing attention due to the emergence of unexpected material properties. As many properties critically depend on the exact twist angle and its spatial homogeneity, there is a need for a fast and non-invasive characterization technique of the local twist angle, to be applied preferably right after stacking. We demonstrate that confocal Raman spectroscopy can be utilized to spatially map the twist angle in stacked bilayer graphene for angles between 6.5° and 8° when using a green excitation laser. The twist angles can directly be extracted from the moiré superlattice-activated Raman scattering process of the transverse acoustic (TA) phonon mode. Furthermore, we show that the width of the TA Raman peak contains valuable information on spatial twist angle variations on length scales below the laser spot size of ∼500 nm.

A unique degree of freedom in stacked two-dimensional (2D) materials is the twist angle, θ, between the crystal lattice of adjacent layers. The interlayer twist angle leads to the formation of superstructures with large periodicity, so-called moiré patterns, which have been shown to strongly influence the electronic, optical and phononic properties of twisted homo- and heterostructures [1–5]. In particular, structures of twisted graphene layers show a wide range of interesting phenomena including superconductivity, ferromagnetism, Fermi velocity reduction or the formation of topological channels [2, 3, 6–13]. Many of these phenomena can be explored in twisted bilayer graphene (tBLG) near the so-called magic angle, around $\theta \sim 1.1°$. Larger twist angles enable a fine control over the Fermi velocity [14] and the tailoring of optoelectronic properties [15, 16]. For example, tunable van Hove singularities allow for twist angle controlled visible and near-infrared absorption enhancement, making twisted bilayer graphene interesting for sensitive wavelength selective photo-detectors [15]. All these effects not only strongly depend on θ, but are further affected by spatial variations and local gradients in θ, which may occur during the sample fabrication and have been shown to yield strong unscreened in-plane electric fields or change the local band structure [17]. It is therefore important to establish non-invasive characterization techniques for the spatial probing of twist angles, which can be used during device fabrication and help to link physical phenomena to twist angles and spatial twist angle variations.

Different experimental techniques have been employed to spatially resolve variations in θ, such as (a) transmission electron microscopy [18, 19], (b) atomic force microscopy (AFM) [20–22],

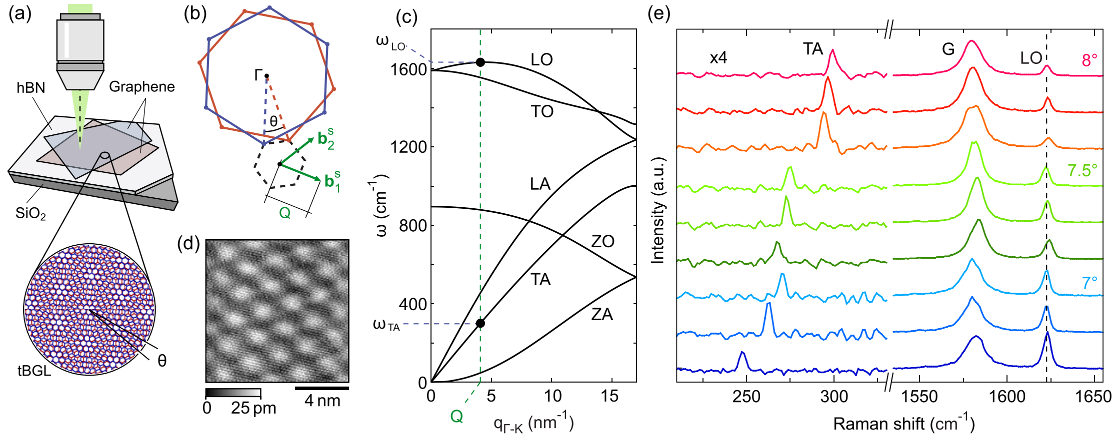

Figure 1. (a) Schematics of the experimental setup for spatial Raman mapping of tBLG on hBN. The lower inset highlights the formed moiré pattern for a given twist angle θ. (b) A mini Brillouin zone with reciprocal lattice vectors $\mathbf{b}^{s}_{1,2}$ emerges due to the additional periodicity of the superlattice. (c) Phonon dispersion along the Γ–K direction highlighting the three acoustic (A) and three optical (O) phonon branches. The vertical green dotted line indicates the momentum Q provided by the superlattice, which allows additional Raman scattering. (d) Scanning tunneling microscopy image with atomic resolution of fabricated tBLG structure with a twist angle of 7.5° as deduced from the moiré periodicity. (e) Raman spectra taken on three different tBLG samples with different nominal twist angels: 8° (red/orange traces), 7.5° (green) and 7° (blue). For each sample three spectra on different positions are shown highlighting the different twist angle sensitivity of the superlattice-induced Raman peaks (TA and LO). Here, the Raman signal of the silicon background is subtracted for clarity.

(c) scanning tunneling spectroscopy [23–29], (d) tip-enhanced Raman spectroscopy [30], (e) azimuthal scanning electron microscopy [31], (f) scanning microwave impedance microscopy [32], and (g) scanning superconducting quantum interference device (SQUID) microscopy [17]. However, these techniques are either not applicable for tBLG fully encapsulated in hexagonal boron nitride (hBN) (a)–(d), lack θ sensitivity (e), (f), have low throughput (a), (c), (d), (g), require low temperatures (g) or specialized sample preparation (a), (c), (d), (g). In contrast, confocal Raman spectroscopy, as a promising optical characterization technique to determine θ, is fast, spatially-resolved, non-invasive and allows to probe buried layers. This method has been recently employed to image θ in twisted transition-metal dichalcogenides [33]. Its capabilities to resolve θ in graphene are however limited, when considering the energy, i.e. frequency of the major G, D and 2D Raman modes of graphene, due to their weak dependence on θ [30, 34–36].

Here we utilize superlattice-activated Raman scattering processes leading to additional Raman peaks that have been shown to exhibit a large energy dependence on the twist angle [37–42] and thus promise a high precision in determining θ. By performing spatially-resolved confocal Raman spectroscopy on twisted bilayer graphene we show that the superlattice-induced transverse acoustic (TA) Raman peak at $\omega_{\mathrm{TA}} \approx 275\,\mathrm{cm}^{-1}$ can be used to spatially map the twist angles with a precision to resolve changes in θ better than 0.01° for twist angles ranging from 6.5° to 8°. This high precision enables us to spatially resolve minute twist angle variations within the device, making confocal Raman mapping a very valuable method for assessing the twist angle homogeneity. Furthermore, we show that the observed TA peak width, Γ_{TA}, can be used as a measure of nanometer-scale twist angle variations smaller than the size of the laser spot, which allows for the identification of regions with a homogeneous twist angle.

We start by recalling the physical processes behind the twist angle-related Raman peaks in stacked bilayer graphene [37–39, 43]. When two graphene layers are stacked with a twist angle θ between their lattices, a superlattice is formed in real space (see lattice structure in figure 1(a)). In reciprocal space, this additional periodicity results in a new mini-Brillouin zone (dotted lines in figure 1(b)) with lattice vectors $\mathbf{b}^{s}_{1,2}(\theta)$ of length

$$Q(\theta) = |\mathbf{b}^{s}_{1,2}(\theta)| = \frac{8\pi}{\sqrt{3}a}\sin\left(\frac{\theta}{2}\right), \qquad (1)$$

where $a = 0.247\,\mathrm{nm}$ is the lattice parameter of graphene. This reduction in Brillouin zone size can be viewed as the ability of the superlattice to provide momenta of multiples of its reciprocal lattice vectors $\mathbf{b}^{s}_{1,2}(\theta)$. As a result, the momentum selection rules for Raman scattering allow probing of additional phonon modes that are located at $\Gamma \pm \mathbf{b}^{s}_{1,2}(\theta)$, i.e. these modes become Raman active [37–39, 43]. The respective frequencies of these superlattice-induced Raman peaks depend on θ due to the dispersion of the phonon modes (see figure 1(c)) and the relation between Q and θ (equation (1)). Although the path in reciprocal space defined by $\mathbf{b}^{s}_{1,2}(\theta)$ slightly deviates from the path along Γ–K, we use the phonon dispersion along this high-symmetry axis in our analysis.

The accuracy of this approximation is discussed below and in the supplementary information. It is important to emphasize that these Raman peaks result from resonant Raman scattering processes, i.e. their respective intensities depend on the combination of the twist angle and laser energy used for the Raman experiments.

The investigated van der Waals heterostructures were built using the tear and stack method [44, 45] and consist of an hBN crystal (20–30 nm thick) with tBLG of the respective nominal twist angle on top (see figure 1(a)). To achieve this stacking orientation, the heterostructures were fabricated using a polydimethylsiloxane (PDMS)/polyvinyl alcohol stamp to first pick up a hBN flake followed by two graphene sheets torn from the same flake. In the next step, the hBN/tBLG heterostructure is flipped by depositing it on a PDMS/poly(bisphenol A carbonate) stamp with the tBLG lying on the polymer. After this step, the heterostructure is transferred to a $\mathrm{Si}^{++}/\mathrm{SiO}_2$ substrate and the tBLG is lying on top of the hBN crystal. The fabrication procedure is described in detail in the supplemental information. Prior to the Raman measurements, we employed an AFM cleaning step [46, 47] to remove residual polymers from the surface of the tBLG. In figure 1(d) we show a scanning tunneling microscopy (STM) image of such a tBLG sample, demonstrating that we indeed obtain clean samples. Furthermore, a periodicity is observed that can be attributed to the formation of a moiré pattern between the graphene layers with a twist angle of 7.5° [48].

In our twisted bilayer graphene samples we find that the superlattice-induced TA and longitudinal optical (LO) Raman peaks appear most prominently in samples built with twist angles between 6.5° and 8°. This is in line with an analysis that combines the optical resonance conditions with symmetry considerations of the electron–phonon interaction as outlined in [49]. For a green laser with a photon energy of 2.33 eV and twist angles near 7°, we accordingly identify the superlattice-induced peaks as the result of an intralayer process excited near the K-point, where the required crystal momentum for the phonon transition matches the length of the mini-Brillouin zone $Q(\theta)$ [37–39]. These energy and momentum considerations would in principle allow all phonon branches to become Raman-active, but due to symmetry considerations only phonons from the TA and LO branch are allowed to partake in intralayer transitions and thus become observable in our measurement [50, 51]. Figure 1(e) shows several representative Raman spectra measured on samples with nominal (n) twist angles of $\theta_\mathrm{n} = 7°$, 7.5° and 8°. Although both modes can also be observed at larger and lower twist angles with lower intensities, we restrict our study to this angle range with large peak intensities. This allows for short data acquisition times and, hence, Raman images with high spatial resolution [39].

The most striking observation in figure 1(e) is the large change in the frequency of the Raman TA peak for different twist angles, compared to the Raman G and LO peak. The strong variation of the Raman TA peak position can be traced back to the large dispersion $\partial\omega_\mathrm{TA}/\partial q$ of the TA branch, as shown in figure 1(c). Importantly, we also observe strong variations of ω_TA within each sample, e.g. up to shifts of 25 cm^{-1} for the sample with $\theta_\mathrm{n} = 7°$ (blue spectra in figure 1(e)), indicating spatial inhomogeneities in θ.

For mapping the twist angle and studying its spatial homogeneity we focus on the spatial dependence of ω_TA and the strong dependence of ω_TA on θ. We present spatial Raman maps of the sample built with a nominal twist angle of $\theta_\mathrm{n} = 7°$, which shows the strongest θ variations in figure 1(e). In figures 2(a) and (b) we show an optical image and a phase image taken by AFM, respectively, showing the finished tBLG sample with $\theta_\mathrm{n} = 7°$. The dotted line outlines the region of tBLG. As indicated by the arrow, the stack got ruptured along several directions during fabrication. The ruptures are well visible in the Raman map of the 2D peak width Γ_2D in figure 2(c). The 2D peak width is known to be strongly influenced by the electronic band-structure-changes between graphene and tBLG [34, 52], which results in an overall narrow line width for (effective) single-layer graphene and a broader line width for bilayer graphene. The small line width and a decrease in G peak intensity (not displayed) along the ruptures (yellowish color) shows the presence of single-layer graphene, indicating that the ruptures and cracks are predominantly present only in one of the graphene sheets in the tBLG sample. However, the Raman G peak position ω_G in figure 2(d) is spatially quite homogeneous, indicating that there are no large amounts of residual strain or doping within the heterostructure [53–55].

In contrast, ω_TA (figure 2(e)) varies significantly and forms distinct domains mostly delimited by ruptures and cracks. Thanks to the homogeneity in ω_G, we exclude strain and doping as the origin of these variations in ω_TA and therefore conclude that variations in ω_TA result from changes in the twist angle θ. We note that the ω_TA mode cannot be extracted for all regions of the tBLG. This might either be due to disordered folding of the graphene sheets near the edges or due to local twist angle values beyond the accessible range. We next convert the ω_TA values to twist angles θ by inverting equation (1) and using the phonon band structure of graphene. To verify this relation, we first compare the mean values of ω_TA obtained from the three samples to the phonon dispersion along Γ–K, where $q_{\Gamma-\mathrm{K}}$ is converted to a twist angle θ. As shown in figure 2(f), we find a good agreement between the mean ω_TA of our three samples

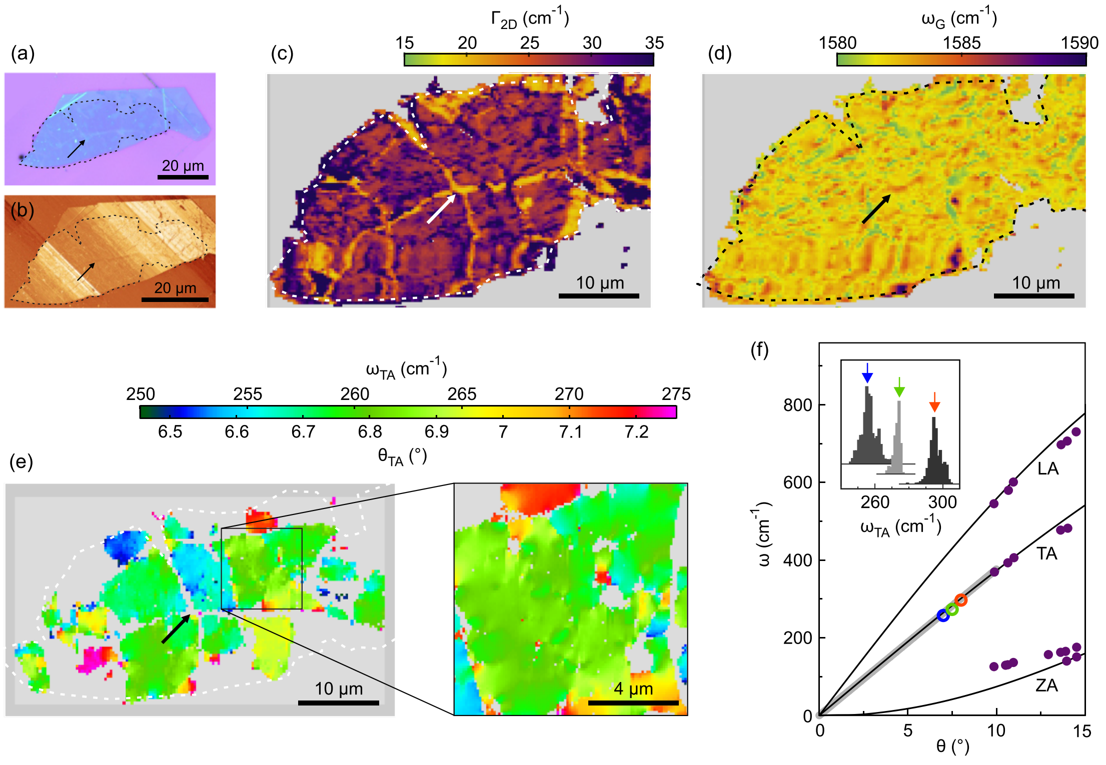

Figure 2. (a) Optical image of tBLG ($\theta_n = 7°$) on hBN (large blue crystal). The dashed lines indicate the extent of the tBLG region. (b) Phase channel of an AFM image of the same heterostructure. The arrow marks a ruptured area of the tBLG. (c) The width of the Raman 2D peak Γ_{2D} highlights folds and cracks within one graphene layer, as indicated e.g. by the arrow. (d) The position of the Raman G peak ω_G shows only minor variations over the entire sample, ruling out strong doping and strain variations. (e) Left panel: the position of the Raman TA peak ω_{TA} shows large spatial variation and the formation of distinct domains between the cracks and folds. Right panel: close-up of the square displayed in the left panel, showing ω_{TA} variations within one 'domain'. (f) Phonon dispersion along the Γ–K direction, where $q_{\Gamma-K}$ is converted to θ via equation (1). The colored circles represent the mean positions of ω_{TA} of the three samples (see inset) built with twist angles of $\theta_n \approx 7°, 7.5°, 8°$. The color code corresponds to figure 1(e). The purple dots are taken from [37]. The bold gray line is a linear fit to ω_{TA} for $\theta < 10°$. The inset shows histograms of ω_{TA} extracted from the Raman maps of the three different samples (see colored arrows).

and the phonon dispersion, when using $\theta_n = 7°, 7.5°$ and 8° as targeted during fabrication. This finding is consistent with previous studies [37] (see purple dots in figure 2(f)) and verifies the θ-dependence of ω_{TA}, which allows to invert $\omega_{TA}(\theta)$ and thus directly translate the ω_{TA} into θ_{TA}. The index of θ_{TA} indicates that the twist angle is determined via the ω_{TA} to θ relation in figure 2(f), in contrast to the nominal twist angle θ_n defined during fabrication. In figure 2(e) we directly converted the ω_{TA} scale bar into a θ_{TA} scale bar using the theoretical phonon dispersion. It shows that even within the same tBLG stack aimed at $\theta_n = 7°$, there are large spatial variations in θ_{TA} ranging from 6.5° to 7.3°.

To estimate the accuracy and precision to determine the twist angle by this technique, we linearize $\omega_{TA}(\theta)$ in this angle regime (see bold gray line in figure 2(f)) to obtain a simple expression of the twist angle given by $\theta_{TA} \approx 0.0265° \cdot \omega_{TA}/\mathrm{cm}^{-1}$. By comparing our theoretical dispersion with earlier experiments [56–59] (see supplementary information), we estimate that there is an uncertainty of ≈9% on the slope of $0.0265°/\mathrm{cm}^{-1}$. This translates into a ≈9% uncertainty on the *absolute* value of the twist angle in figure 2(e). To determine the precision of our method, which defines our ability to resolve *changes* in the twist angle as a function of position, we analyze all the fitting results for the map in figure 2(e) and obtain an average 95% confidence interval for the peak position of $\approx 0.25\ \mathrm{cm}^{-1}$. Using the expression above and taking into account the uncertainty in the slope, we expect that our precision is better than 0.01°. This high precision allows us to map minute twist angle variations within the sample as shown in figure 2(e), which is a key result of this work.

Twist angle variations not only occur near ruptures, cracks or folds in the heterostructure, but also within otherwise continuous regions of tBLG, as illustrated by the close-up shown in figure 2(e). This is in agreement with previous findings using different characterization techniques [13, 17, 31–33], but makes it difficult to directly compare twist angle values extracted from Raman spectroscopy data and from STM images. This is mainly because of difficulties in identifying the exact same locations with both methods. It is worth noting that in one case investigated, good agreement was found within the margins of error (for more details, see

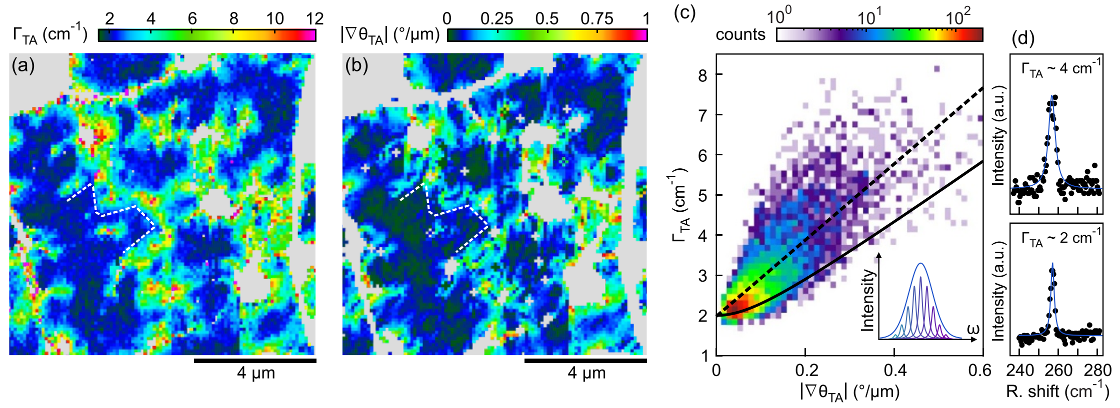

Figure 3. (a) Width of the Raman TA peak Γ_{TA}. (b) Numeric gradient of θ_{TA}, calculated from the close-up in figure 2(e). The white dashed line in (a) and (b) is a guide to the eye to allow for easy comparison. (c) Two-dimensional histogram of the correlation between Γ_{TA} and $|\nabla\theta_{\mathrm{TA}}|$. For clarity both values are spatially averaged over their next-nearest neighbors. The black dashed line shows a linear fit to the experimental data. The black line shows the expected broadening due to a homogeneous gradient in θ_{TA}, i.e. in ω_{TA}. The inset illustrates the peak broadening effect due to $|\nabla\theta_{\mathrm{TA}}|$. The colored lines represent the spectral contribution of different positions within the laser spot. The pink line is the averaged Raman intensity detected at the spectrometer. (d) Two representative Raman spectra of the TA mode with respective Lorentzian fits.

supplementary information). The information on θ_{TA} obtained via confocal Raman spectroscopy is suitable for a fast characterization of tBLG stacks, or for the preselection of high-quality areas with high θ homogeneity for subsequent device fabrication.

The spatial resolution of this method is, however, limited by the laser spot size, making it difficult to resolve twist angle variations smaller than the spot size. To obtain further insight into twist angle variations on length scales smaller than the laser spot size, we can analyze the width of the Raman TA peak, Γ_{TA}. Figure 3(a) shows a map of Γ_{TA} corresponding to the magnified area shown in figure 2(e). We note that these measurements were taken with a grating of 2400 lines mm^{-1} to allow for the high energy resolution needed for the line width analysis. As can be seen in figure 3(a), there are substantial variations in Γ_{TA} extending over a range of 2–10 cm^{-1} (see also two representative Raman spectra with respective Lorentzian fits in figure 3(d)). The largest line widths are observed in areas of large variations in ω_{TA}, i.e. in θ_{TA} (compare to figure 2(e)). We highlight this by numerically calculating the magnitude of the gradient $|\nabla\theta_{\mathrm{TA}}|$ as shown in figure 3(b) (for an easy comparison see white dashed lines in figures 3(a) and (b)). To evaluate the correlation in more detail, we plot Γ_{TA} versus $|\nabla\theta_{\mathrm{TA}}|$ in figure 3(c), where we employed next-nearest neighbor averaging. The correlation map suggests that the increase in Γ_{TA} in areas of large $|\nabla\theta_{\mathrm{TA}}|$ is caused by locally averaging various spectra of different θ_{TA}, i.e. ω_{TA}, within the laser spot. This effect is similar to the known strain variation-induced broadening of the 2D Raman peak in graphene [54, 60]. The inset of figure 3(c) illustrates how this statistical averaging effect broadens the TA peak.

To further verify that the peak broadening can be attributed to statistical averaging, we perform a numerical estimate of the expected Γ_{TA} for a given gradient $|\nabla\theta_{\mathrm{TA}}|$. This is done by convolving the Gaussian shape of the laser spot with a Lorentzian peak describing the Raman TA mode with a linearly varying ω_{TA}, which corresponds to a constant $|\nabla\theta_{\mathrm{TA}}|$ [54]. The Gaussian peak is assumed to have a full width at half maximum of 520 nm (corresponding to the measured laser spot size, as shown in the supplementary information), and we use the lowest experimentally measured Γ_{TA} as the intrinsic width $\Gamma_{\mathrm{TA}}(|\nabla\theta| \approx 0) \approx 2\,\mathrm{cm}^{-1}$. After this convolution, we use a Lorentzian fit to determine Γ_{TA} of the convolved peak. The result is shown as black line in figure 3(c), representing the Raman TA peak width if the gradient $|\nabla\theta_{\mathrm{TA}}|$ is homogeneous within the laser spot.

Since any inhomogeneities would lead to a TA peak broadening, we expect this line to represent a lower bound which agrees well with the experimental data in figure 3(c). Data points close to the black line represent areas of the tBLG where the broadening Γ_{TA} is dominated by twist angle variations extending to length scales larger than the laser spot size (520 nm). Values of Γ_{TA} above this line correspond to areas with large variations in θ on length scales smaller than the spot size, which cannot be spatially-resolved and thus do not contribute to $|\nabla\theta_{\mathrm{TA}}|$. To quantify the empirically found correlation of Γ_{TA} and $|\nabla\theta_{\mathrm{TA}}|$ in figure 3(c), we perform a linear fit to our experimental data as shown by the black dashed line in figure 3(c). We find $\Gamma_{\mathrm{TA}}(|\nabla\theta| \approx 0) = 1.97 \pm 0.01\,\mathrm{cm}^{-1}$ and a slope of $\beta = 9.47 \pm 0.08\,\mathrm{cm}^{-1}/(^\circ/\mu\mathrm{m})$. The average twist angle gradient within our laser spot is thus given by $|\overline{\nabla\theta_{\mathrm{TA}}}| = 0.106\ \ (^\circ/\mu\mathrm{m}) \cdot(\Gamma_{\mathrm{TA}} - 1.97\,\mathrm{cm}^{-1})/(\mathrm{cm}^{-1})$, where Γ_{TA} is the experimentally measured TA peak width. This analysis demonstrates that measuring the Raman TA peak position and width allows to spatially map the twist angle and the twist angle variations in tBLG.

In our study, we have focused on tBLG with $\theta \approx 6.5°$–$8°$ due to the resonant effects enhancing the intensity of the TA peak. To characterize samples with smaller or larger twist angles, the resonance conditions have to be considered [38, 39, 49, 61]. For small twist angles $\theta \lesssim 4°$, the excitation energy of the laser can be reduced into the infrared regime. Close to the magic angle, however, the electronic band structure of graphene flattens [6], which may reduce the resonance energy even further than the ~0.5 eV predicted by theory [39, 50]. To circumvent this problem, small twist angles may also be accessed through electron–phonon processes close to the M point, which requires larger excitation energies in the UV regime [41, 49]. Lattice relaxation effects are another important consideration at small twist angles, since these can alter the phonon dispersion [62]. While the method can still provide qualitative information on twist angle inhomogeneities, for the absolute value of θ one needs to replace the single-layer graphene (SLG) phonon dispersion with an appropriate calculation. Our method can also be extended to larger angles with the 2.33 eV excitation, since the TA peak can be observed for $\theta > 15°$ due to an interlayer electron–phonon process close to the K point [37, 38].

Our method for determining the twist angle is also interesting for benchmarking different fabrication techniques that are aimed to reduce twist angle variations. Different approaches have emerged to improve the fabrication of twisted bilayer graphene, for example by using pyramid-shaped polymer stamps [63], pre-cutting the graphene by local anodic oxidation or laser cutting [64, 65], and mechanical cleaning by AFM [13]. By constructing samples in the range of 6.5°–8°, our method can quantify whether certain techniques improve the twist angle uniformity in twisted bilayer graphene. This also makes our work relevant for improving the fabrication techniques to make high-quality twisted bilayer graphene near and at the magic angle.

In conclusion, we used confocal Raman spectroscopy to spatially map the twist angle in tBLG within a range of 6.5°–8°. The Raman TA peak, activated by the additional periodicity in the tBLG allows probing minute changes in the twist angle with a precision better than 0.01° and a spatial resolution of ~500 nm. Furthermore, we have shown that Γ_{TA} is a measure of the twist angle variations on length scales below the laser spot size and can be used to estimate the average twist angle gradient. We expect that the properties of twist angle homogeneity investigated here will play a critical role in the understanding and controlling of material properties of twisted van der Waals heterostructures. In short, our work makes spatially-resolved confocal Raman spectroscopy an important tool for the characterization of tBLG and the bench-marking of different fabrication methods.

Data availability statement

The data that support the findings of this study are openly available at the following URL/DOI: 10.5281/zenodo.6631559.

Acknowledgments

This project has received funding from the European Union's Horizon 2020 research and innovation programme under Grant Agreement No. 881603 (Graphene Flagship) and from the European Research Council (ERC) under Grant Agreement No. 820254, under FLAG-ERA Grant TATTOOS by the Deutsche Forschungsgemeinschaft (DFG, German Research Foundation)—437214324, the Deutsche Forschungsgemeinschaft (DFG, German Research Foundation) under Germany's Excellence Strategy—Cluster of Excellence Matter and Light for Quantum Computing (ML4Q) EXC 2004/1-390534769, through DFG (STA 1146/12-1 and Mo 858/15-1), and by the Helmholtz Nano Facility [66]. Growth of hexagonal boron nitride crystals was supported by the Elemental Strategy Initiative conducted by the MEXT, Japan, Grant Number JPMXP0112101001, JSPS KAKENHI Grant Numbers JP20H00354 and the CREST(JPMJCR15F3), JST. L W acknowledges financial support from the Fond National de Recherche, Luxembourg via Project INTER/19/ANR/13376969/ACCEPT.

ORCID iDs

J Sonntag https://orcid.org/0000-0002-6066-0436
K Watanabe https://orcid.org/0000-0003-3701-8119
L Wirtz https://orcid.org/0000-0001-5618-3465
M Morgenstern https://orcid.org/0000-0002-3993-6880
B Beschoten https://orcid.org/0000-0003-2359-2718
R J Dolleman https://orcid.org/0000-0002-6976-8443
C Stampfer https://orcid.org/0000-0002-4958-7362

References

[1] Wang L *et al* 2020 Correlated electronic phases in twisted bilayer transition metal dichalcogenides *Nat. Mater.* **19** 861–6
[2] Yin L-J, Qiao J-B, Wang W-X, Zuo W-J, Yan W, Xu R, Dou R-F, Nie J-C and He L 2015 Landau quantization and Fermi velocity renormalization in twisted graphene bilayers *Phys. Rev.* B **92** 201408
[3] Luican A, Li G Reina A, Kong J, Nair R R, Novoselov K S, Geim A K and Andrei E Y 2011 Single-layer behavior and its breakdown in twisted graphene layers *Phys. Rev. Lett.* **106** 126802
[4] Lin M-L *et al* 2018 Moiré phonons in twisted bilayer MoS_2 *ACS Nano* **12** 8770–80

[5] Huang X *et al* 2021 Correlated insulating states at fractional fillings of the WS_2/WSe_2 moiré lattice *Nat. Phys.* **17** 715–9

[6] Cao Y, Fatemi V, Fang S, Watanabe K, Taniguchi T, Kaxiras E and Jarillo-Herrero P 2018 Unconventional superconductivity in magic-angle graphene superlattices *Nature* **556** 43–50

[7] Cao Y *et al* 2018 Correlated insulator behaviour at half-filling in magic-angle graphene superlattices *Nature* **556** 80–84

[8] Liu X *et al* 2020 Tunable spin-polarized correlated states in twisted double bilayer graphene *Nature* **583** 221–5

[9] Rickhaus P *et al* 2018 Transport through a network of topological channels in twisted bilayer graphene *Nano Lett.* **18** 6725–30

[10] Rickhaus P *et al* 2019 Gap opening in twisted double bilayer graphene by crystal fields *Nano Lett.* **19** 8821–8

[11] Rickhaus P *et al* 2020 The electronic thickness of graphene *Sci. Adv.* **6** eaay8409

[12] de Vries F K *et al* 2020 Combined minivalley and layer control in twisted double bilayer graphene *Phys. Rev. Lett.* **125** 176801

[13] Lu X *et al* 2019 Superconductors, orbital magnets and correlated states in magic-angle bilayer graphene *Nature* **574** 653–7

[14] Nishi H, Matsushita Y-I and Oshiyama A 2017 Band-unfolding approach to moiré-induced band-gap opening and Fermi level velocity reduction in twisted bilayer graphene *Phys. Rev.* B **95** 085420

[15] Yin J *et al* 2016 Selectively enhanced photocurrent generation in twisted bilayer graphene with van Hove singularity *Nat. Commun.* **7** 10699

[16] Pogna E A A, Miao X, von Dreifus D, Alencar T V, Moutinho M V O, Venezuela P, Manzoni C, Ji M, Cerullo G and de Paula A M 2021 Angle-tunable intersubband photoabsorption and enhanced photobleaching in twisted bilayer graphene *Nano Res.* **14** 2797–804

[17] Uri A *et al* 2020 Mapping the twist-angle disorder and Landau levels in magic-angle graphene *Nature* **581** 47–52

[18] Alden J S, Tsen A W, Huang P Y, Hovden R, Brown L, Park J, Muller D A and McEuen P L 2013 Strain solitons and topological defects in bilayer graphene *Proc. Natl Acad. Sci. USA* **110** 11256–60

[19] Yoo H *et al* 2019 Atomic and electronic reconstruction at the van der Waals interface in twisted bilayer graphene *Nat. Mater.* **18** 448–53

[20] Gallagher P *et al* 2016 Switchable friction enabled by nanoscale self-assembly on graphene *Nat. Commun.* **7** 10745

[21] McGilly L J *et al* 2020 Visualization of moiré superlattices *Nat. Nanotechnol.* **15** 580–4

[22] Sunku S S *et al* 2018 Photonic crystals for nano-light in moiré graphene superlattices *Science* **362** 1153–6

[23] Li G, Luican A, Lopes dos Santos J M B, Castro Neto A H, Reina A, Kong J and Andrei E Y 2010 Observation of van Hove singularities in twisted graphene layers *Nat. Phys.* **6** 109–13

[24] Yankowitz M, Xue J, Cormode D, Sanchez-Yamagishi J D, Watanabe K, Taniguchi T, Jarillo-Herrero P, Jacquod P and LeRoy B J 2012 Emergence of superlattice Dirac points in graphene on hexagonal boron nitride *Nat. Phys.* **8** 382–6

[25] Kerelsky A *et al* 2019 Maximized electron interactions at the magic angle in twisted bilayer graphene *Nature* **572** 95–100

[26] Choi Y *et al* 2019 Electronic correlations in twisted bilayer graphene near the magic angle *Nat. Phys.* **15** 1174–80

[27] Xie Y, Lian B, Jäck B, Liu X, Chiu C-L, Watanabe K, Taniguchi T, Bernevig B A and Yazdani A 2019 Spectroscopic signatures of many-body correlations in magic-angle twisted bilayer graphene *Nature* **572** 101–5

[28] Jiang Y, Lai X, Watanabe K, Taniguchi T, Haule K, Mao J and Andrei E Y 2019 Charge order and broken rotational symmetry in magic-angle twisted bilayer graphene *Nature* **573** 91–95

[29] Hattendorf S, Georgi A, Liebmann M and Morgenstern M 2013 Networks of ABA and ABC stacked graphene on mica observed by scanning tunneling microscopy *Surf. Sci.* **610** 53–58

[30] Gadelha A C *et al* 2021 Localization of lattice dynamics in low-angle twisted bilayer graphene *Nature* **590** 405–9

[31] Sushko A *et al* 2019 High resolution imaging of reconstructed domains and moire patterns in functional van der Waals heterostructure devices (arXiv:1912.07446)

[32] Lee K *et al* 2020 Ultrahigh-resolution scanning microwave impedance microscopy of moiré lattices and superstructures *Sci. Adv.* **6** eabd1919

[33] Lin K-Q, Holler J, Bauer J M, Parzefall P, Scheuck M, Peng B, Korn T, Bange S, Lupton J M and Schüller C 2021 Large-scale mapping of moiré superlattices by hyperspectral Raman imaging *Adv. Mater.* **33** 2008333

[34] Kim K, Coh S, Tan L Z, Regan W, Yuk J M, Chatterjee E, Crommie M F, Cohen M L, Louie S G and Zettl A 2012 Raman spectroscopy study of rotated double-layer graphene: misorientation-angle dependence of electronic structure *Phys. Rev. Lett.* **108** 246103

[35] Gupta A K, Tang Y, Crespi V H and Eklund P C 2010 Nondispersive Raman *D* band activated by well-ordered interlayer interactions in rotationally stacked bilayer graphene *Phys. Rev.* B **82** 241406

[36] Havener R W, Zhuang H, Brown L, Hennig R G and Park J 2012 Angle-resolved Raman imaging of interlayer rotations and interactions in twisted bilayer graphene *Nano Lett.* **12** 3162–7

[37] Campos-Delgado J, Cançado L G, Achete C A, Jorio A and Raskin J-P 2013 Raman scattering study of the phonon dispersion in twisted bilayer graphene *Nano Res.* **6** 269–74

[38] Jorio A and Cançado L G 2013 Raman spectroscopy of twisted bilayer graphene *Solid State Commun.* **175–176** 3–12

[39] Carozo V, Almeida C M, Ferreira E H M, Cançado L G, Achete C A and Jorio A 2011 Raman signature of graphene superlattices *Nano Lett.* **11** 4527–34

[40] Righi A, Costa S D, Chacham H, Fantini C, Venezuela P, Magnuson C, Colombo L, Bacsa W S, Ruoff R S and Pimenta M A 2011 Graphene moiré patterns observed by umklapp double-resonance Raman scattering *Phys. Rev.* B **84** 241409

[41] Righi A, Venezuela P, Chacham H, Costa S D, Fantini C, Ruoff R S, Colombo L, Bacsa W S and Pimenta M A 2013 Resonance Raman spectroscopy in twisted bilayer graphene *Solid State Commun.* **175–176** 13–17

[42] Wang Y *et al* 2013 Resonance Raman spectroscopy of G-line and folded phonons in twisted bilayer graphene with large rotation angles *Appl. Phys. Lett.* **103** 123101

[43] He R, Chung T-F, Delaney C, Keiser C, Jauregui L A, Shand P M, Chancey C C, Wang Y, Bao J and Chen Y P 2013 Observation of low energy Raman modes in twisted bilayer graphene *Nano Lett.* **13** 3594–601

[44] Kim K *et al* 2016 van der Waals heterostructures with high accuracy rotational alignment *Nano Lett.* **16** 1989–95

[45] Cao Y, Luo J Y, Fatemi V, Fang S, Sanchez-Yamagishi J D, Watanabe K, Taniguchi T, Kaxiras E and Jarillo-Herrero P 2016 Superlattice-induced insulating states and valley-protected orbits in twisted bilayer graphene *Phys. Rev. Lett.* **117** 116804

[46] Goossens A M, Driessen S C M, Baart T A, Watanabe K, Taniguchi T and Vandersypen L M K 2012 Gate-defined confinement in bilayer graphene-hexagonal boron nitride hybrid devices *Nano Lett.* **12** 4656–60

[47] Kim Y, Herlinger P, Taniguchi T, Watanabe K and Smet J H 2019 Reliable postprocessing improvement of van der Waals heterostructures *ACS Nano* **13** 14182–90

[48] Shallcross S, Sharma S, Kandelaki E and Pankratov O A 2010 Electronic structure of turbostratic graphene *Phys. Rev.* B **81** 165105

[49] Eliel G S N *et al* 2018 Intralayer and interlayer electron–phonon interactions in twisted graphene heterostructures *Nat. Commun.* **9** 1221

[50] Moutinho M V O, Eliel G S N, Righi A, Gontijo R N, Paillet M, Michel T, Chiu P-W, Venezuela P and

Pimenta M A 2021 Resonance Raman enhancement by the intralayer and interlayer electron–phonon processes in twisted bilayer graphene *Sci. Rep.* **11** 1–9

[51] Malard L M, Guimarães M H D, Mafra D L, Mazzoni M S C and Jorio A 2009 Group-theory analysis of electrons and phonons in *N*-layer graphene systems *Phys. Rev.* B **79** 125426

[52] Graf D, Molitor F, Ensslin K, Stampfer C, Jungen A, Hierold C and Wirtz L 2007 Spatially resolved Raman spectroscopy of single- and few-layer graphene *Nano Lett.* **7** 238–42

[53] Mohiuddin T M G *et al* 2009 Uniaxial strain in graphene by Raman spectroscopy: *G* peak splitting, Grüneisen parameters and sample orientation *Phys. Rev.* B **79** 205433

[54] Neumann C *et al* 2015 Raman spectroscopy as probe of nanometre-scale strain variations in graphene *Nat. Commun.* **6** 8429

[55] Stampfer C, Molitor F, Graf D, Ensslin K, Jungen A, Hierold C and Wirtz L 2007 Raman imaging of doping domains in graphene on SiO_2 *Appl. Phys. Lett.* **91** 241907

[56] Cong X, Li Q-Q, Zhang X, Lin M-L, Wu J-B, Liu X-L, Venezuela P and Tan P-H 2019 Probing the acoustic phonon dispersion and sound velocity of graphene by Raman spectroscopy *Carbon* **149** 19–24

[57] Oshima C, Aizawa T, Souda R, Ishizawa Y and Sumiyoshi Y 1988 Surface phonon dispersion curves of graphite (0001) over the entire energy region *Solid State Commun.* **65** 1601–4

[58] Siebentritt S, Pues R, Rieder K-H and Shikin A M 1997 Surface phonon dispersion in graphite and in a lanthanum graphite intercalation compound *Phys. Rev.* B **55** 7927–34

[59] Yanagisawa H, Tanaka T, Ishida Y, Matsue M, Rokuta E, Otani S and Oshima C 2005 Analysis of phonons in graphene sheets by means of HREELS measurement and *ab initio* calculation *Surf. Interface Anal.* **37** 133–6

[60] IEC TS 62607-6-6:2021 2021 Nanomanufacturing—key control characteristics—part 6-6: graphene—strain uniformity: Raman spectroscopy International Electrotechnical Commission 1st edn (available at: https://webstore.iec.ch/publication/34162)

[61] Carozo V *et al* 2013 Resonance effects on the Raman spectra of graphene superlattices *Phys. Rev.* B **88** 085401

[62] Ochoa H 2019 Moiré-pattern fluctuations and electron-phason coupling in twisted bilayer graphene *Phys. Rev.* B **100** 155426

[63] Gadelha A C *et al* 2021 Twisted bilayer graphene: a versatile fabrication method and the detection of variable nanometric strain caused by twist-angle disorder *ACS Appl. Nano Mater.* **4** 1858–66

[64] Li H, Ying Z, Lyu B, Deng A, Wang L, Taniguchi T, Watanabe K and Shi Z 2018 Electrode-free anodic oxidation nanolithography of low-dimensional materials *Nano Lett.* **18** 8011–5

[65] Park J M, Cao Y, Watanabe K, Taniguchi T and Jarillo-Herrero P 2021 Flavour Hund's coupling, Chern gaps and charge diffusivity in moiré graphene *Nature* **592** 43–48

[66] Albrecht W, Moers J and Hermanns B 2017 HNF-Helmholtz nano facility *J. Large-Scale Res. Facil. JLSRF* **3** 112